AGU ADVANCING EARTH AND SPACE SCIENCE

Geophysical Research Letters®

RESEARCH LETTER
10.1029/2022GL102102

Sea Ice Melt Pond Fraction Derived From Sentinel-2 Data: Along the MOSAiC Drift and Arctic-Wide

Hannah Niehaus[1], Gunnar Spreen[1], Gerit Birnbaum[2], Larysa Istomina[2], Evelyn Jäkel[3], Felix Linhardt[4], Niklas Neckel[2], Niels Fuchs[5], Marcel Nicolaus[2], Tim Sperzel[3], Ran Tao[2], Melinda Webster[6], and Nicholas Wright[7]

[1]Institute of Environmental Physics, University of Bremen, Bremen, Germany, [2]Helmholtz Centre for Polar and Marine Research, Alfred Wegener Institute Bremerhaven, Bremerhaven, Germany, [3]Faculty of Physics and Earth Science, Leipzig University, Leipzig, Germany, [4]Department of Geography, Kiel University, Kiel, Germany, [5]Institute of Oceanography, University of Hamburg, Hamburg, Germany, [6]Polar Science Center, Applied Physics Laboratory, University of Washington, Seattle, WA, USA, [7]Thayer School of Engineering, Dartmouth College, Hanover, NH, USA

Key Points:

- Algorithm to extract melt pond and open water areas from Sentinel-2 imagery with maximum uncertainty of 6%
- Exceptional early melt pond formation on MOSAiC Central Observatory, summer 2020, compared to broader vicinity
- High spatial and temporal variability of melt pond fraction on local and regional scales

Supporting Information:

Supporting Information may be found in the online version of this article.

Correspondence to:

H. Niehaus,
niehaus@uni-bremen.de

Citation:

Niehaus, H., Spreen, G., Birnbaum, G., Istomina, L., Jäkel, E., Linhardt, F., et al. (2023). Sea ice melt pond fraction derived from Sentinel-2 data: Along the MOSAiC drift and Arctic-wide. *Geophysical Research Letters*, *50*, e2022GL102102. https://doi.org/10.1029/2022GL102102

Received 18 NOV 2022
Accepted 16 FEB 2023

Abstract Melt ponds forming on Arctic sea ice in summer significantly reduce the surface albedo and impact the heat and mass balance of the sea ice. Therefore, their areal coverage, which can undergo rapid change, is crucial to monitor. We present a revised method to extract melt pond fraction (MPF) from Sentinel-2 satellite imagery, which is evaluated by MPF products from higher-resolution satellite and helicopter-borne imagery. The analysis of melt pond evolution during the MOSAiC campaign in summer 2020, shows a split of the Central Observatory (CO) into a level ice and a highly deformed ice part, the latter of which exhibits exceptional early melt pond formation compared to the vicinity. Average CO MPFs are 17% before and 23% after the major drainage. Arctic-wide analysis of MPF for years 2017–2021 shows a consistent seasonal cycle in all regions and years.

Plain Language Summary In the Arctic summer, puddles of surface melt water, called melt ponds, form on the sea ice. These melt ponds reduce the ability of the surface to reflect the sunlight. Instead, they absorb more solar energy and pave the way into the ocean beneath where the energy is also absorbed. Thus, it is important to know where these melt ponds develop and what fraction of the surface they cover. To investigate this, we present a classification algorithm that is used to extract the areal fraction of melt ponds from satellite measurements. The special focus of this study is the MOSAiC campaign in summer 2020, where the research vessel Polarstern drifted with an ice floe for 1 year. We can see a separation of this floe into two parts. One of them shows melt pond formation much earlier than the other. This is because of different ice age and surface properties. Additionally, we use the classification algorithm to analyze the differences of melt pond fraction between different dates and regions in the Arctic.

1. Introduction

During the Arctic summer, melting of snow and sea ice forms pools of melt water on top of the sea ice (Untersteiner, 1961). The areal fraction of sea ice covered by these melt ponds is called melt pond fraction (MPF) and exhibits high temporal and spatial variability (Perovich et al., 2002; Polashenski et al., 2012). Peak MPFs of 60%–80% (Eicken et al., 2004; Maykut et al., 1992) depend on ice type, topography, and location (Istomina, Heygster, Huntemann, Marks, et al., 2015; Polashenski et al., 2012). Typical values of MPFs in summer in the central Arctic range from 15% to 40% (Istomina, Heygster, Huntemann, Marks, et al., 2015; Rösel & Kaleschke, 2011). Melt ponds on sea ice significantly reduce its broadband and spectral albedo (Light et al., 2022; Malinka et al., 2018) affecting the heat and mass balance due to an increase of solar absorption within and an enhancement of transmission through the ice into the Arctic Ocean (Light et al., 2008; Nicolaus et al., 2012). However, global climate models still lack a comprehensive representation of melt ponds (Dorn et al., 2018; Hunke et al., 2013; Zhang et al., 2018). This is caused by the complexity and variability of melt pond formation and evolution and the mismatch between true and observational scales.

There are numerous efforts to advance the understanding of melt pond physics based on in-situ (e.g., Light et al., 2008; Nicolaus et al., 2012), airborne (e.g., Buckley et al., 2020; Miao et al., 2015), and high resolution ($\mathcal{O}$(m)) satellite measurements (e.g., Istomina, Heygster, Huntemann, Marks, et al., 2015; Markus et al., 2002). Due to the limited availability of observational data, most research is focused on case studies and is often used for

validation purposes of medium-resolution and low-resolution satellite observations, which cover larger areas and longer time periods (e.g., Peng et al., 2022; Zege et al., 2015).

We have generalized an algorithm by Wang et al. (2020) to extract MPF from a data set of 31 optical satellite measurements of the Copernicus Sentinel-2 mission. Using the generalized approach, we (a) analyzed the MPF along the track of the Multidisciplinary drifting Observatory for the Study of Arctic Climate (MOSAiC) from June 14 to July 27, 2020, (b) produced more data sets of MPF in the Arctic, for example, for validation purposes of lower resolution MPF products or evaluation of models, and (c) studied the local and temporal variability of MPF in the Arctic.

2. Study Sites and Data Sets

2.1. Study Sites

In 2019–2020, the year-long Arctic research expedition MOSAiC of the research vessel *Polarstern* measured and analyzed sea ice, atmospheric, ocean, bio-geochemical, and ecological processes throughout a full seasonal cycle (Nicolaus et al., 2022; Rabe et al., 2022; Shupe et al., 2022). Webster et al. (2022) present a detailed analysis of melt pond evolution on the MOSAiC Central Observatory (CO) primarily based on in-situ transect measurements. Krumpen et al. (2021) show the first insights into optical satellite imagery of the CO. We expand on these investigations by analyzing the full available Sentinel-2 data set covering the drifting position of the MOSAiC CO, from June to July 2020. For the investigation of the classification algorithm performance and the presentation of pan-Arctic MPF variability, satellite measurements of other locations are included in our analysis for 2017 to 2021.

2.2. Sentinel-2 Satellite Imagery

We use Top-of-Atmosphere (TOA) reflectances supplied by the Sentinel-2A and 2B satellites operated by the European Space Agency (https://scihub.copernicus.eu/dhus/). The satellites provide coverage of latitudes up to 82.8° with a swath width of 290 km and revisit time of 5 days. However, the availability of suitable scenes is compromised by prevalent cloud contamination typical for the Arctic summer. Thus, the number of available Sentinel-2 scenes during MOSAiC is strongly limited. The MultiSpectral Instrument (MSI) measures TOA radiances in 13 spectral bands in the visible and near-infrared (NIR) range (440–2,200 nm) with a spatial resolution of 10–60 m (10 m for bands used). These are post-processed to Level-1C TOA reflectances, which are provided in orthorectified quality with correction for the disparity of the incoming solar radiation and a distinctive cloud mask.

For this study, Sentinel-2 scenes are only considered if the cloud percentage provided with the product is less than 1%. In addition, a combination of bands 8 and 11 (842 and 1,610 nm) is used to check for cloud contamination following the criteria described in Istomina et al. (2010). In two cases (July 7 and July 27), a manual correction is applied to account for a constant offset which likely was caused by thin fog. The pool of suitable Sentinel-2 imagery is split into a development set (10 scenes) for tuning the classification algorithm, and another set (21 scenes) for unbiased testing. An overview of all scenes used, their acquisition times, locations, and purposes can be found in Table S5 in Supporting Information S1.

2.3. OSSP Melt Pond Product From SkySat Satellite Imagery

One product used for the classification algorithm evaluation is based on high-resolution (0.5 m) satellite imagery obtained by the Planet SkySat (courtesy of Planet Labs, Inc.) satellite platform. The SkySat mission comprises 21 satellites circling in a non-sun-synchronous orbit at an altitude of 450 km to achieve a spatial resolution of 0.5 m of the orthorectified product, which has a minimum swath width of 5.5 km. The data contain measurements of the reflected radiance in four spectral bands. These cover the wavelengths required for RGB imagery and the NIR. Based on the Open Source sea ice Processing (OSSP) algorithm (Wright & Polashenski, 2019), Wright et al. (2021) provide a classification of these data into four surface type classes: (a) open water, (b) melt ponds and submerged ice, (c) thin ice, and (d) thick ice. For the comparison with the Sentinel-2 data, classes (c) and (d) are combined into one sea ice class, and (b) corresponds to the melt pond class.

2.4. Airborne Imagery-Based Melt Pond Product

The helicopter-borne sea ice surveys conducted during the summer of the MOSAiC campaign provide high-resolution RGB imagery acquired with a Canon EOS 1D Mark III camera with wide-angle lens. This imagery is stitched and provided as orthomosaics with a resolution of 0.5 m (Neckel et al., 2022). The main classes deduced from the RGB imagery are (a) open water, (b) melt ponds, (c) submerged ice, and (d) snow and ice. For our purpose, classes (b) and (c) are summarized as "melt pond" class for the comparison with the products derived from SkySat and Sentinel-2 satellite imagery and class (d) corresponds to the "ice class." The estimated error of the product is 2%. Further information about the processing is given in Text S1 in Supporting Information S1.

3. Methodology

3.1. Classification of Sentinel-2 Imagery

Melt pond sizes on sea ice range from cm^2 to km^2 (Perovich et al., 2002) with a majority smaller or in the range of the Sentinel-2 footprint of 10 m pixel size. For this reason, a binary classification is not sufficient and a spectral unmixing approach is necessary to estimate the MPF. In this paper, MPFs are computed as the pond area divided by the ice (ponded plus not ponded) area.

The *LinearPolar* Algorithm by Wang et al. (2020) was developed for extracting MPF from small subsets (less than 2 km edge length) of Sentinel-2 scenes. We generalized the fundamental approach for the application to extended regions (larger than 50 km length) and a wider variability of scenes.

The algorithm uses band 2 (blue, *B2*) and 8 (NIR, *B8*) of the Sentinel-2 instrument with central wavelengths of 490 and 842 nm, respectively. This is because of the significant difference between the spectral behavior of ice, melt pond, and open water surfaces at these wavelengths (Rösel et al., 2012; Wang et al., 2020). Note that the sensor measures spectral reflectance and there is a conceptual difference to albedo. In the following, however, the term albedo is used for consistency with other literature. Whereas melt ponds have a much lower albedo in the NIR (0.1–0.2) than in visible wavelengths (0.4–0.7), unponded ice shows little changes in albedo in the range of *B2* (0.7–1.0) and only a slight decrease toward *B8* (0.6–0.9) (Istomina, Heygster, Huntemann, Schwarz, et al., 2015; Malinka et al., 2018). This spectral behavior is dictated by the amount of liquid water in the surface layer. Water is quite transparent below 500 nm and increasingly absorbing above, defining the albedo's sensitivity to the scattering properties of the underlying ice (Grenfell & Maykut, 1977; Perovich, 1996). This leads to a considerable variability of the albedo of ice surfaces depending on the melt progress. Open water shows a constant albedo of less than 0.1 (Pohl et al., 2020) in the visible and NIR range. Based on these differences, the scatterplot in Figure 1a displays three major modes. The most confined one is the open water mode with low values for both *B2* and the difference between bands 2 and 8 (*B2-B8*), due to its constant spectral behavior. The largest mode presents all types of ice surfaces featuring a large variability due to the differences in ice scattering properties and in the amount of liquid water. However, there is a straight line defining an upper limit where the brightest pixels of pure, unponded ice are located. The third mode exhibits another edge where the pixels with 100% ponds are aligned. Based on those modes two lines, named *ice axis* and *pond axis*, are defined serving as principal components for a coordinate transformation. Fixed axes are used for the whole data set to ascertain a robust classification independent of the image details and subset size. The choice of the axes is conducted on a set of 10 scenes, which comprise a variety of melt stages and feature different compositions of the surface constituents. The Sentinel-2 scenes used for defining the axes, thus forming the training data set of the classification algorithm, are marked with a *D* in the *purpose* column in Table S5 in Supporting Information S1.

Subsequently, the two-dimensional Cartesian scatterplot is transformed into polar coordinates. The transformation is based on the approach by Wang et al. (2020) and explained in Text S2 in Supporting Information S1. This leads to the two axes becoming parallel, as visualized in Figure 1b θ is associated with the MPF of each pixel, assuming a linear transition between the 100% axes for ponds and ice. r relates to the different spectral behavior of darker and brighter ice surfaces or pond types. Thus, the distinct mode of dark, open water can be clearly identified at low values of r and a cutoff value for open water areas is defined. All pixels with values r smaller than the water cutoff value are set to 0 MPF and are excluded from the assignment of MPF linearly depending on the value of θ. This yields an estimate of the open water area. The open water cutoff value can be clearly identified for every single scene. However, it can vary between scenes depending

10.1029/2022GL102102

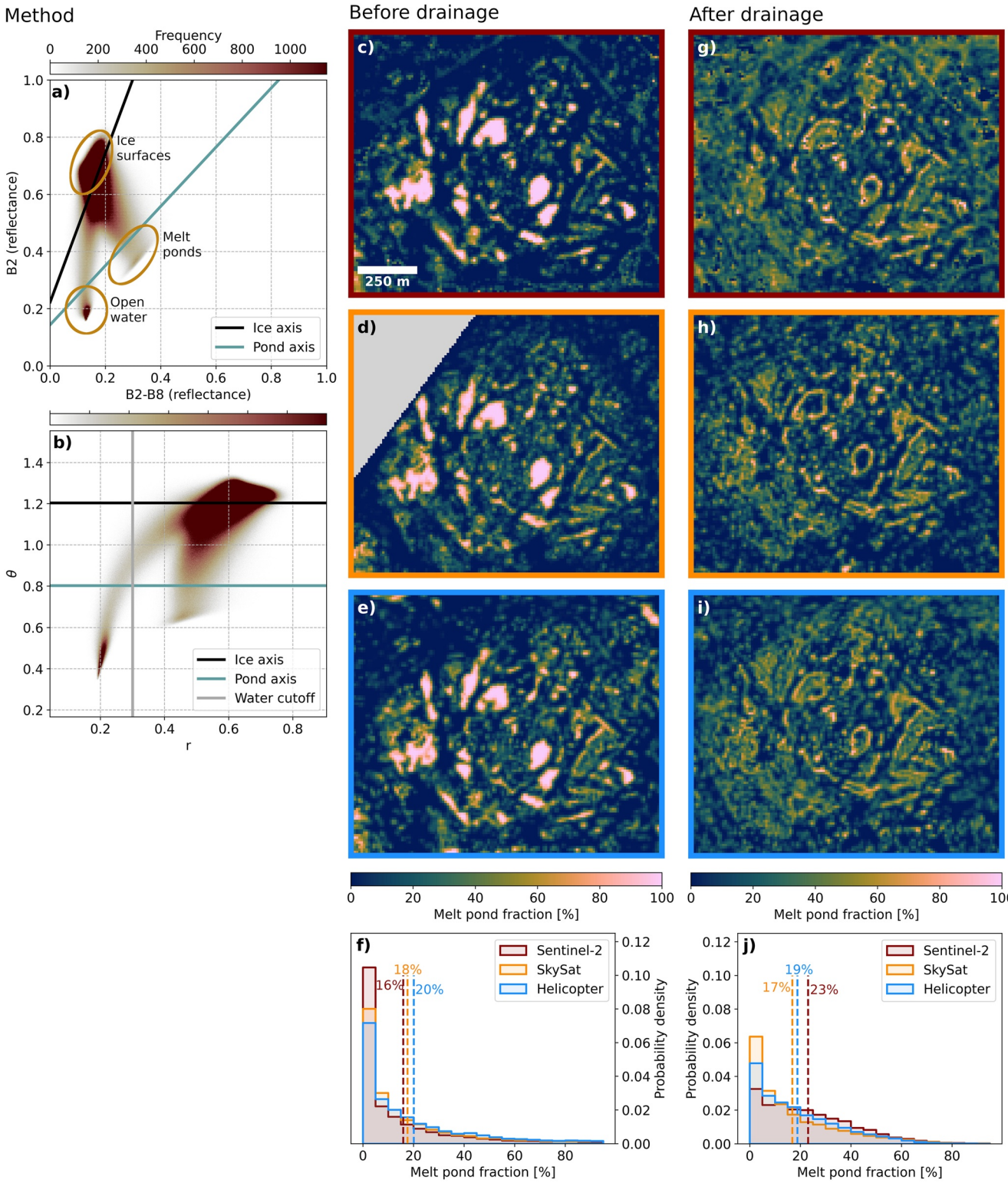

Figure 1. Left: Two-dimensional density plots of Sentinel-2 reflectances of (a) band 2 (*B2*) and the difference between bands 2 and 8 (*B2–B8*) and (b) the transformed coordinates r and θ. The color scale indicates the frequency of the appearance of value pairs. The ice and pond axes are marked in black and red, respectively. The open water cutoff threshold is denoted by the gray vertical line in (b). This example shows the results for scene T31XEL on June 30, 2022. Middle and right: MPF maps derived from Sentinel-2 ((c) and (g)) and down-scaled MPF maps from SkySat ((d) and (h)) and Helicopter observations ((e) and (i)) together with histograms of the MPF distributions ((f) and (j)). The dashed lines in (f) and (j) mark the mean MPFs. Panels (c)–(f) show measurements from June 30 (Sentinel-2 and Helicopter) and July 1 (SkySat), before the drainage of the ponds started. Panels (g)–(j) show measurements from July 22, after the major drainage period. The colored frames of the maps indicate the different data sets according to the colors in the histograms.

on the existence of open water and the dominant ice types. Therefore, a default value for the cutoff is set to $r = 0.35$. The suitability of this threshold is checked for each sample individually. An adjustment of 0.30–0.38 is made if there is a significant amount of pixels with $\theta >$ *pond axis* but $r <$ *water cutoff* that can not be assigned to open water areas.

3.2. Validation With High-Resolution Imagery

The Sentinel-2 MPF is compared with MPFs derived from helicopter-borne and higher-resolution SkySat satellite imagery, which both have a resolution of 0.5 m. The higher resolution three-class products are scaled down to the resolution of 10 m of Sentinel-2 and converted into an MPF by taking the average of the binned pixels. For the collocation of the different data sets, the ice drift within the time offset between the acquisition times is approximated using the GNSS position of *Polarstern*. However, the open water area can change considerably even in short time periods. The position of the research vessel is then used as reference point to define the areas to be compared. Figure 1 displays the Sentinel-2 melt pond classification results in comparison with the MPF products from SkySat and airborne imagery for two dates: before and after the major drainage (Webster et al., 2022) during which meltwater flushed vertically through the ponded ice. In Figure S3 in Supporting Information S1, the comparison for July 7, where melting has progressed, is presented. The results shown in Figures 1c–1f combine June 30 (Sentinel-2 and Helicopter) and July 1 (SkySat). Sentinel-2 imagery is available for both days showing little changes. Thus the combination of these days for a pre-drainage comparison of melt pond classification results is feasible. The post-drainage MPFs all stem from the same day, July 22. This results in time differences (relative to the Sentinel-2 acquisition) of +28:37 hr and −6:05 hr pre-drainage and +5:23 hr and +1:13 hr post-drainage, for SkySat and helicopter-borne measurements, respectively.

In both cases, the dominant sea ice and pond features are clearly visible in all products and agree well regarding the MPFs. It is evident that the higher-resolution products resolve more small-scale pond features even with the downsampled resolution shown here. This is the reason the histogram of Sentinel-2 MPF shows a significantly higher peak at minimum MPF values before the drainage (Figure 1f). After the drainage, the probability for pixels with minimum MPF values in the Sentinel-2 product is much lower than for the other products (Figure 1j). Due to the overall shift of surface conditions from ice partly covered with distinct ponds to a water-saturated surface with smaller unponded ice areas, this is attributed to the resolution difference as well. With ponds draining and advanced melt, the surface conditions become more spatially complex, with small-scale alternation of surface types causing higher uncertainties in MPF. However, the agreement shown visually and by statistics is excellent with the mean difference being smaller than 7%. We conclude that implementing the above described classification algorithm to Sentinel-2 reflectance measurements is reasonable with an uncertainty increasing with melt due to the spatial heterogeneity of surface conditions. From the differences between Sentinel-2 MPFs, and higher resolution evaluation MPFs, the uncertainty of the product is estimated to be maximum of 6%. Before melt ponds start draining, the uncertainty is even below 4% as the melt pond features are more distinct and better resolvable.

4. Results and Discussion

4.1. Case Study—Melt Pond Fraction Along MOSAiC Drift Track

Figure 2a shows true color composites and their classification of all the Sentinel-2 observations with little or no cloud contamination along the MOSAiC drift track in summer 2020. The MPF maps are presented for the small segment of the MOSAiC CO (1.2 km × 1.4 km) and for an extended area of 3 km × 3.5 km centered on the floe. On July 1, the extent of the cloud-free scene is limited. In Figure S4 in Supporting Information S1, four more dates with observations that are disturbed by clouds and thus not useful for quantitative analysis are displayed for the visual impression of MPF evolution.

At the time of the first observation (June 21), shown in Figure 2a, the MOSAiC CO already features large, distinct melt ponds of different colors whereas the neighboring ice floes scarcely exhibit melt ponds. Earlier observations from Sentinel-2 are not available as the MOSAiC site was at latitudes higher than the limitations of the satellite mission. Webster et al. (2022) date the melt onset on the CO to the end of May with melt ponds visible on the whole floe on May 28. The short melt period was accompanied by rainfall and followed by a period of freezing

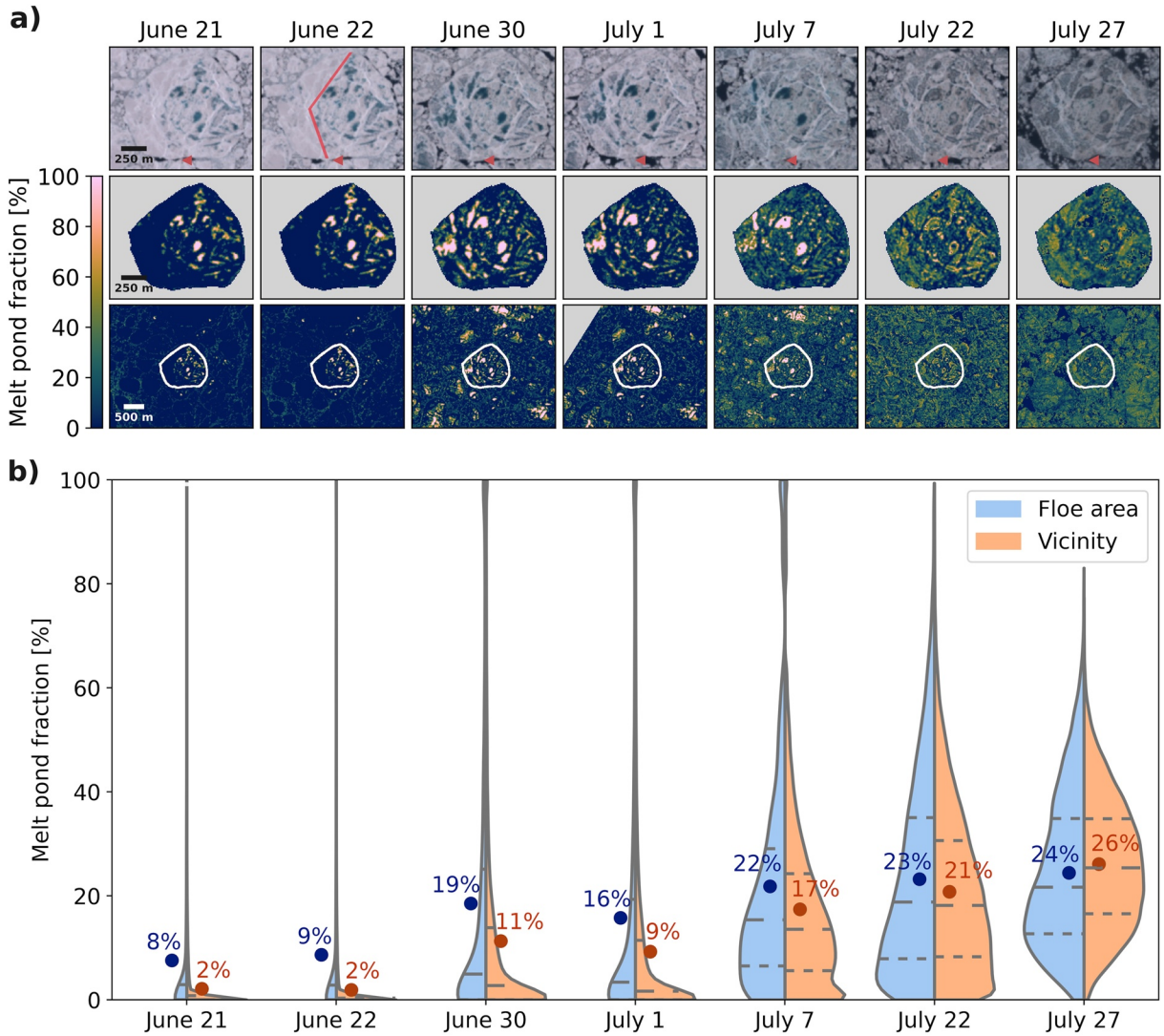

Figure 2. Melt pond fraction (MPF) evolution along the MOSAiC drift track. (a) Upper row: Sentinel-2 true color composites of the MOSAiC Central Observatory (CO) area with the Polarstern position marked by the red triangles. The red line on June 22 marks the observed split of the CO. Middle row: MPF classification results in % for the CO. Bottom row: MPFs of the CO's vicinity, displayed in the same colorscale as above. The indicated CO area is excluded from the comparison. (b) Probability density functions of the MPF distribution for the CO area (blue) and vicinity (orange). The circles mark the mean MPFs for the two areas, with the values given aside. The dashed lines mark the medians and upper and lower quantiles.

and fresh snowfall. This event pre-conditioned the surface for later pond formation, visible in the observations on June 18 (Figure S4 in Supporting Information S1), 21, and 22. In the first two columns in Figure 2, the true color composite and MPF maps for the latter two dates are presented. The mean values of MPF at the MOSAiC CO are 8% and 9%, and in the vicinity, 2% and 2%, for June 21 and 22, respectively. By vicinity, we mean the area shown in the bottom row, excluding the CO floe area shown in the middle row. The difference between the melt pond development stages of the MOSAiC floe and neighboring floes is even more distinct when inspecting the statistical distribution of MPF values, presented in Figure 2b. For both, the vicinity and the floe area, the distribution covers the full range of MPFs with a peak at low MPF values. This peak is narrower for the vicinity area. Interestingly, the MOSAiC CO can be divided into two regions: one features large melt ponds, the other is almost pond-free similar to the neighboring floes. The MOSAiC CO was characterized by strong deformation and high surface roughness in parts of the CO (Nicolaus et al., 2022). While ridges are expected to limit the extent of melt ponds and thus reduce MPFs (Eicken et al., 2004; Untersteiner, 1961), the deformed region was the one with large melt ponds and higher MPF. This relation between ice types and pond formation has also been observed by Webster et al. (2015) and can be attributed to the accumulation of melt water in depressions and the local snow

distribution. Thus, in the early melting stage, a division of the CO into two parts with highly deformed ice and more melt ponds, and more level-ice with less melt ponds, as observed here, is reasonable. Nevertheless, later in the melt season flat ice shows similar high MPFs.

About 1 week later, on June 30 and July 1, melt ponds have extended, the more level region of the MOSAiC CO is heavily ponded now and also the neighboring floes exhibit enhanced pond formation. The overall appearance of the surface in the top row of Figure 2a is darker, which may be attributed to the complete melt of snow by June 25 (Lei et al., 2022) leading to an increased humidity of the surface and the emergence of sediment in the ice. The distribution of MPF (Figure 2b) is broadened and for both areas, tapers above 40%. However, there is a slight increase toward 100%. The mean values on the MOSAiC CO are 19% and 16% and on the neighboring floes 11% and 9% for June 30 and July 1, respectively. These differences between the 2 days and regions are smaller than the estimated uncertainty of the product. However, the classification is self-contained. Thus, relative changes between days may be detected even below the algorithm uncertainty.

July 7 is the last observation where large, distinct melt ponds are visible. However, ponds close to the floe edge have already drained. They become connected to the ocean by lateral channels which enable the outflow of water while the more centered and isolated ponds remain intact (Polashenski et al., 2012; Webster et al., 2022). By July 18 (Figure S4 in Supporting Information S1) and latest July 22, all large melt ponds have drained. The ponds become more interconnected and smaller due to the development of vertical drainage channels (Flocco et al., 2010; Perovich et al., 2021). Most of them cannot be separated anymore at the 10-m resolution, which darkens the overall appearance of the ice resulting in a broad MPF distribution during this later melt stage. This darkening might be strengthened by sediments trapped in the ice coming to the surface with advanced melt. Webster et al. (2022) date the major drainage period between July 10 and 12, which would cause an MPF reduction. Lei et al. (2022) report an increase of ice/snow melt between July 10 and 20 of +0.14 m. This is in agreement with the observation of exceptionally warm and moist conditions in July and August 2020 (Rinke et al., 2021). Despite the high permeability of the ice after drainage, the enhanced surface melt causes a lateral expansion of existing ponds and thus a slight increase of the mean MPF in the period from July 7 to 27. However, the distribution of MPF values is changing significantly. Fully pond-covered pixels diminish as well as those pixels with no ponds at all. The ice becomes water-saturated leading to an overall darkening of the surface (Eicken et al., 2002).

The satellite-derived MPFs exhibit a similar evolution as the in-situ transect measurements conducted by Webster et al. (2022) but show slightly higher values. The largest difference occurred on June 30 and was 11%. This difference may be attributable to the fact that both SkySat and Sentinel-2 could sample the largest interior ponds on the CO, which were 100+ m in diameter (Webster et al., 2022), whereas the transect sampled the edge of the CO, where melt ponds remained relatively smaller due to continual lateral drainage. A study of MPFs on multiyear ice by Perovich et al. (2002) shows fast and early (around June 16) evolution of melt ponds and slow development later in the season. This agrees with our observation for the deformed part of the CO which already features melt ponds on June 21. On the opposite, Istomina, Heygster, Huntemann, Schwarz, et al. (2015) present MPF evolution on multiyear and first-year ice for 9 years showing a steeper but slightly later increase of MPF for first-year ice compared to multiyear ice. However, this study underlines the strong inter-annual variability. The differences in MPF evolution between the two CO areas, that is, within close vicinity but different ice types, indicate a strong dependence of the timing of pond evolution on the surface roughness (Webster et al., 2015) besides the expected impact of limiting the MPF later in the season.

4.2. Spatial and Temporal MPF Variability

With our classification method, the spatial variability of MPF can also be analyzed on a larger scale. Figure 3 presents the mean MPF values of a set of 30 Sentinel-2 observations at different times and locations in the Arctic. An overall start of pond formation in mid-June to early July is visible with considerably increasing MPFs in the first week of July in all three regions: Canadian Arctic, Fram Strait, and Siberian Arctic. In our analysis, the evolution peaks around July 8 and decreases quickly first, and more slowly toward late summer. This temporal evolution is in good agreement with a comparison of different pan-Arctic melt pond products performed by Peng et al. (2022). Note that the variability in our time series partly results from combining observations from different years and regions with different conditions (atmosphere, surface, and ice) which influence pond formation significantly (e.g., Li et al., 2020; Liu et al., 2015).

For the Fram Strait (orange), the data set shows the most continuous evolution (Figure 3) as it monitors the same ice floes following the MOSAiC drift whose MPF evolution is discussed in Section 4.1. In the Canadian Arctic

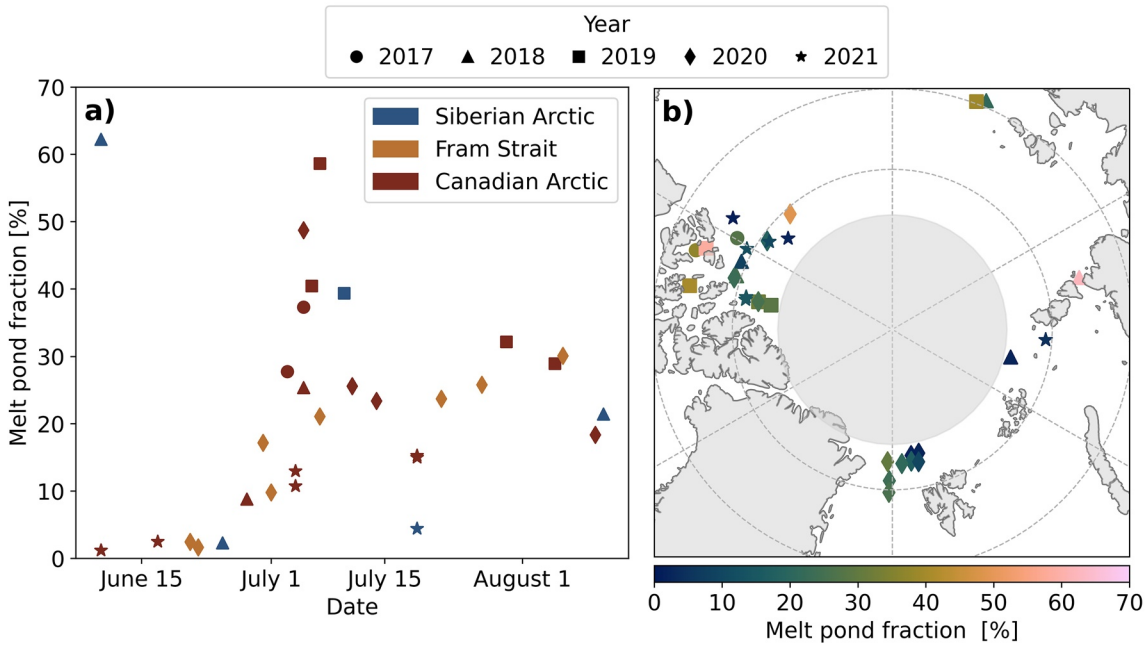

Figure 3. Sentinel-2 derived melt pond fractions (MPFs) plotted against date (a) and on a pan-Arctic map (b). The shape of the markers depicts the year of observation. (a) The color of the markers shows a regional assignment. (b) The color scale indicates the MPF, the gray circle shows the area where Sentinel-2 is not measuring.

(red), some of the highest MPFs are detected. This is likely because the landfast ice is less deformed enabling the flooding of large areas once melt ponds have formed (Landy et al., 2014; Yackel et al., 2000). This might also be the reason for the heavily ponded subset in early summer (June 10) in the Siberian Arctic (blue), which is between Bolshevik Island and the mainland apart from being at relatively low latitudes. The results for the Siberian Arctic scatter the most and do not show a gradual evolution over the summer. The scatter between different regions can be of similar magnitude as the scatter between different years of a particular region. Thus, more satellite scenes assisted by airborne measurements would be necessary for further analysis.

5. Conclusions

This study expands the spatial component of melt pond evolution observed at the MOSAiC CO, and enables a discussion of the CO's representation of the broader vicinity. This is a unique time series of MPF evolution on a regional scale, including different ice types, different roughness areas and their impact on initial melt pond development and drainage later in the season. Despite the resolution of 10 m, the overall development and drainage of melt ponds are well monitored and in agreement with in-situ observations (Webster et al., 2022). However, the estimated uncertainty of 4% and 6% before and after the pond drainage, eventually exceeds the MPF differences between days. An increase of uncertainty with the development of lateral and vertical drainage channels can be assumed. Strong spatial variability is observed even within the MOSAiC CO based on different ice topography, showing a segmentation of the CO into two parts: one with level ice and one with highly deformed ice. There is a large timing offset in melt pond formation between these two areas. Even though an increased surface roughness limits the spreading of ponds and thus reduces MPF (Eicken et al., 2004) later in the season, in the earlier melt stage it shows an opposite effect (Webster et al., 2015). The deformed ice exhibits earlier ponding and makes the MOSAiC floe non-representative for the melting in the vicinity at this stage. The earlier episodic ponding and refreezing might influence this timing difference in summer pond formation and is to be investigated (Thielke et al., 2022). At the beginning of July, the mean MPF on the CO amounts to 16% and at the end of July, after pond drainage, to 24%. The study of pan-Arctic MPF reveals large variability between regions and years underlining the need of improved MPF data sets. The presented algorithm can be applied to any Sentinel-2 measurements of sea ice/ocean surfaces to extract melt pond and open water fractions. The presented subsets are available on PANGAEA and can serve as reference for the validation and evaluation of low-resolution pan-Arctic melt pond products.

Acronyms

CO	central observatory
EOS	electro-optical system
GNSS	global navigation satellite system
MOSAiC	multidisciplinary drifting observatory for the study of arctic climate
MPF	melt pond fraction
MSI	multiSpectral instrument
NIR	near-infrared
RGB	red-green-blue
SSL	surface scattering layer
TOA	top of the atmopshere

Data Availability Statement

- The Sentinel-2 satellite imagery is available at the Copernicus Open access Hub of the European Space Agency (ESA) under: https://scihub.copernicus.eu/dhus/#/home
- The MPF product based on the Sentinel-2 imagery will be available on PANGAEA (https://doi.org/10.1594/PANGAEA.950885)
- The optical orthomosaics are available on PANGAEA (https://doi.pangaea.de/10.1594/PANGAEA.949433)
- The OSSP-derived satellite melt pond fractions (Wright & Polashenski, 2020) for MOSAiC are available at the Arctic Data Center under: N. Wright et al. (2021), https://doi.org/10.18739/A2696ZZ9W

Acknowledgments
This work was funded by the German Research Foundation (DFG, Deutsche Forschungsgemeinschaft)—Project-ID 268020496—TRR 172 within the collaborative research project (AC)^3; on Arctic Amplification and through the Priority Program SPP 1158 (Grant 424326801). The authors thank the European Space Agency for providing the Sentinel-2 satellite data. MW conducted this work under NASA's New Investigator Program in Earth Science (80NSSC20K0658) and National Science Foundation project (2138786). MN was partly funded through the EU Horizon 2020 project Arctic Passion (101003472). NN, GB, and GS were supported by the BMBF IceSense (03F0866A, 03F0866B) project. FL was supported by the German Federal Ministry for Economic Affairs and Energy (BMWi) project ArcticSense (50EE1917A). NF was supported by the German Ministry for Education and Research (BMBF) through the project NiceLABpro (Grant 03F0867A). Part of the data used in this article were produced as part of the international MOSAiC project with the tag MOSAiC20192020 and the Project_ID: AWI_PS122_00. The authors thank all people involved in the expedition of the R/V Polarstern during MOSAiC in 2019–2020, especially HeliService and their pilots, as listed in (Nixdorf et al., 2021). Open Access funding enabled and organized by Projekt DEAL.

References

Buckley, E. M., Farrell, S. L., Duncan, K., Connor, L. N., Kuhn, J. M., & Dominguez, R. T. (2020). Classification of sea ice summer melt features in high-resolution IceBridge imagery. *Journal of Geophysical Research: Oceans*, *125*(5), e2019JC015738. https://doi.org/10.1029/2019jc015738

Dorn, W., Rinke, A., Köberle, C., Dethloff, K., & Gerdes, R. (2018). HIRHAM–NAOSIM 2.0: The upgraded version of the coupled regional atmosphere-ocean-sea ice model for Arctic climate studies. *Geoscientific Model Development Discussions*, 1–30.

Eicken, H., Grenfell, T., Perovich, D., Richter-Menge, J., & Frey, K. (2004). Hydraulic controls of summer Arctic pack ice albedo. *Journal of Geophysical Research: Oceans*, *109*(C8), C08007. https://doi.org/10.1029/2003jc001989

Eicken, H., Krouse, H., Kadko, D., & Perovich, D. (2002). Tracer studies of pathways and rates of meltwater transport through Arctic summer sea ice. *Journal of Geophysical Research: Oceans*, *107*(C10), 8046. https://doi.org/10.1029/2000jc000583

Flocco, D., Feltham, D. L., & Turner, A. K. (2010). Incorporation of a physically based melt pond scheme into the sea ice component of a climate model. *Journal of Geophysical Research: Oceans*, *115*(C8), C08012. https://doi.org/10.1029/2009jc005568

Grenfell, T. C., & Maykut, G. A. (1977). The optical properties of ice and snow in the Arctic Basin. *Journal of Glaciology*, *18*(80), 445–463. https://doi.org/10.1017/s0022143000021122

Hunke, E. C., Hebert, D. A., & Lecomte, O. (2013). Level-ice melt ponds in the Los Alamos sea ice model, CICE. *Ocean Modelling*, *71*, 26–42. https://doi.org/10.1016/j.ocemod.2012.11.008

Istomina, L., Heygster, G., Huntemann, M., Marks, H., Melsheimer, C., Zege, E., et al. (2015). Melt pond fraction and spectral sea ice albedo retrieval from MERIS data—Part 2: Case studies and trends of sea ice albedo and melt ponds in the Arctic for years 2002–2011. *The Cryosphere*, *9*(4), 1567–1578. https://doi.org/10.5194/tc-9-1567-2015

Istomina, L., Heygster, G., Huntemann, M., Schwarz, P., Birnbaum, G., Scharien, R., et al. (2015). Melt pond fraction and spectral sea ice albedo retrieval from MERIS data—Part 1: Validation against in situ, aerial, and ship cruise data. *The Cryosphere*, *9*(4), 1551–1566. https://doi.org/10.5194/tc-9-1551-2015

Istomina, L., von Hoyningen-Huene, W., Kokhanovsky, A., & Burrows, J. (2010). The detection of cloud-free snow-covered areas using AATSR measurements. *Atmospheric Measurement Techniques*, *3*(4), 1005–1017. https://doi.org/10.5194/amt-3-1005-2010

Krumpen, T., von Albedyll, L., Goessling, H. F., Hendricks, S., Juhls, B., Spreen, G., et al. (2021). MOSAiC drift expedition from October 2019 to July 2020: Sea ice conditions from space and comparison with previous years. *The Cryosphere*, *15*(8), 3897–3920. https://doi.org/10.5194/tc-15-3897-2021

Landy, J., Ehn, J., Shields, M., & Barber, D. (2014). Surface and melt pond evolution on landfast first-year sea ice in the Canadian Arctic Archipelago. *Journal of Geophysical Research: Oceans*, *119*(5), 3054–3075. https://doi.org/10.1002/2013jc009617

Lei, R., Cheng, B., Hoppmann, M., Zhang, F., Zuo, G., Hutchings, J. K., et al. (2022). Seasonality and timing of sea ice mass balance and heat fluxes in the Arctic transpolar drift during 2019- 2020. *Elementa*, *10*(1), 000089. https://doi.org/10.1525/elementa.2021.000089

Light, B., Grenfell, T. C., & Perovich, D. K. (2008). Transmission and absorption of solar radiation by Arctic sea ice during the melt season. *Journal of Geophysical Research: Oceans*, *113*(C3), C03023. https://doi.org/10.1029/2006jc003977

Light, B., Smith, M. M., Perovich, D. K., Webster, M. A., Holland, M. M., Linhardt, F., et al. (2022). Arctic sea ice albedo: Spectral composition, spatial heterogeneity, and temporal evolution observed during the MOSAiC drift. *Elementa: Science of the Anthropocene*, *10*(1), 000103. https://doi.org/10.1525/elementa.2021.000103

Li, Q., Zhou, C., Zheng, L., Liu, T., & Yang, X. (2020). Monitoring evolution of melt ponds on first-year and multiyear sea ice in the Canadian Arctic Archipelago with optical satellite data. *Annals of Glaciology*, *61*(82), 154–163. https://doi.org/10.1017/aog.2020.24

Liu, J., Song, M., Horton, R. M., & Hu, Y. (2015). Revisiting the potential of melt pond fraction as a predictor for the seasonal Arctic sea ice extent minimum. *Environmental Research Letters*, *10*(5), 054017. https://doi.org/10.1088/1748-9326/10/5/054017

Malinka, A., Zege, E., Istomina, L., Heygster, G., Spreen, G., Perovich, D. K., & Polashenski, C. (2018). Reflective properties of melt ponds on sea ice. *The Cryosphere*, *12*(6), 1921–1937. https://doi.org/10.5194/tc-12-1921-2018

Markus, T., Cavalieri, D. J., & Ivanoff, A. (2002). The potential of using Landsat 7 ETM+ for the classification of sea-ice surface conditions during summer. *Annals of Glaciology*, *34*, 415–419. https://doi.org/10.3189/172756402781817536

Maykut, G., Grenfell, T., & Weeks, W. (1992). On estimating spatial and temporal variations in the properties of ice in the polar oceans. *Journal of Marine Systems*, *3*(1–2), 41–72. https://doi.org/10.1016/0924-7963(92)90030-c

Miao, X., Xie, H., Ackley, S. F., Perovich, D. K., & Ke, C. (2015). Object-based detection of Arctic sea ice and melt ponds using high spatial resolution aerial photographs. *Cold Regions Science and Technology*, *119*, 211–222. https://doi.org/10.1016/j.coldregions.2015.06.014

Neckel, N., Fuchs, N., Birnbaum, G., Hutter, N., Jutila, A., Buth, L., et al. (2022). Helicopter-borne RGB orthomosaics and photogrammetric digital elevation models from the MOSAiC expedition. https://doi.org/10.1594/PANGAEA.949433

Nicolaus, M., Katlein, C., Maslanik, J., & Hendricks, S. (2012). Changes in Arctic sea ice result in increasing light transmittance and absorption. *Geophysical Research Letters*, *39*(24), L24501. https://doi.org/10.1029/2012gl053738

Nicolaus, M., Perovich, D. K., Spreen, G., Granskog, M. A., von Albedyll, L., Angelopoulos, M., et al. (2022). Overview of the MOSAiC expedition: Snow and sea ice. *Elementa: Science of the Anthropocene*, *10*(1), 000046.

Nixdorf, U., Dethloff, K., Rex, M., Shupe, M., Sommerfeld, A., Perovich, D. K., et al. (2021). MOSAiC extended acknowledgement. *Zenodo*. https://doi.org/10.5281/zenodo.5541624

Peng, Z., Ding, Y., Qu, Y., Wang, M., & Li, X. (2022). Generating a long-term spatiotemporally continuous melt pond fraction dataset for Arctic sea ice using an artificial neural network and a statistical-based temporal filter. *Remote Sensing*, *14*(18), 4538. https://doi.org/10.3390/rs14184538

Perovich, D. K. (1996). *The optical properties of sea ice*. (p. 24). CRREL Monograph 9-61, US Army Corps of Engineers.

Perovich, D. K., Smith, M., Light, B., & Webster, M. (2021). Meltwater sources and sinks for multiyear Arctic sea ice in summer. *The Cryosphere*, *15*(9), 4517–4525. https://doi.org/10.5194/tc-15-4517-2021

Perovich, D. K., Tucker, W., III, & Ligett, K. (2002). Aerial observations of the evolution of ice surface conditions during summer. *Journal of Geophysical Research: Oceans*, *107*(C10), 8048. https://doi.org/10.1029/2000jc000449

Pohl, C., Istomina, L., Tietsche, S., Jäkel, E., Stapf, J., Spreen, G., & Heygster, G. (2020). Broadband albedo of Arctic sea ice from MERIS optical data. *The Cryosphere*, *14*(1), 165–182. https://doi.org/10.5194/tc-14-165-2020

Polashenski, C., Perovich, D. K., & Courville, Z. (2012). The mechanisms of sea ice melt pond formation and evolution. *Journal of Geophysical Research: Oceans*, *117*(C1), C01001. https://doi.org/10.1029/2011jc007231

Rabe, B., Heuzé, C., Regnery, J., Aksenov, Y., Allerholt, J., Athanase, M., et al. (2022). Overview of the MOSAiC expedition: Physical oceanography. *Elementa: Science of the Anthropocene*, *10*(1), 00062. https://doi.org/10.1525/elementa.2021.00062

Rinke, A., Cassano, J. J., Cassano, E. N., Jaiser, R., & Handorf, D. (2021). Meteorological conditions during the MOSAiC expedition: Normal or anomalous? *Elementa: Science of the Anthropocene*, *9*(1), 00023. https://doi.org/10.1525/elementa.2021.00023

Rösel, A., & Kaleschke, L. (2011). Comparison of different retrieval techniques for melt ponds on Arctic sea ice from Landsat and MODIS satellite data. *Annals of Glaciology*, *52*(57), 185–191. https://doi.org/10.3189/172756411795931606

Rösel, A., Kaleschke, L., & Birnbaum, G. (2012). Melt ponds on Arctic sea ice determined from MODIS satellite data using an artificial neural network. *The Cryosphere*, *6*(2), 431–446. https://doi.org/10.5194/tc-6-431-2012

Shupe, M. D., Rex, M., Blomquist, B., Persson, P. O. G., Schmale, J., Uttal, T., et al. (2022). Overview of the MOSAiC expedition: Atmosphere. *Elementa: Science of the Anthropocene*, *10*(1), 00060.

Thielke, L., Fuchs, N., Spreen, G., Tremblay, B., Birnbaum, G., Huntemann, M., et al. (2022). Seasonal predictability of summer melt ponds from winter sea ice surface temperature.

Untersteiner, N. (1961). On the mass and heat budget of arctic sea ice. *Archiv für Meteorologie, Geophysik und Bioklimatologie, Serie A*, *12*(2), 151–182. https://doi.org/10.1007/bf02247491

Wang, M., Su, J., Landy, J., Leppäranta, M., & Guan, L. (2020). A new algorithm for sea ice melt pond fraction estimation from high-resolution optical satellite imagery. *Journal of Geophysical Research: Oceans*, *125*(10), e2019JC015716. https://doi.org/10.1029/2019jc015716

Webster, M. A., Holland, M., Wright, N. C., Hendricks, S., Hutter, N., Itkin, P., et al. (2022). Spatiotemporal evolution of melt ponds on Arctic sea ice: MOSAiC observations and model results. *Elementa: Science of the Anthropocene*, *10*(1), 000072.

Webster, M. A., Rigor, I. G., Perovich, D. K., Richter-Menge, J. A., Polashenski, C. M., & Light, B. (2015). Seasonal evolution of melt ponds on Arctic sea ice. *Journal of Geophysical Research: Oceans*, *120*(9), 5968–5982. https://doi.org/10.1002/2015jc011030

Wright, N., & Polashenski, C. (2019). Open source sea-ice processing algorithm v2.3. *Zenodo*. https://doi.org/10.5281/zenodo.3551033

Wright, N., Webster, M., & Polashenski, C. (2021). Melt pond maps around the Multidisciplinary drifting Observatory for the Study of Arctic Climate (MOSAiC) drifting station derived from high resolution optical imagery. Retrieved from https://arcticdata.io/catalog/view/

Wright, N. C., & Polashenski, C. M. (2020). How machine learning and high-resolution imagery can improve melt pond retrieval from MODIS over current spectral unmixing techniques. *Journal of Geophysical Research: Oceans*, *125*(2), Porticoe, 2019JC015569. https://doi.org/10.1029/2019jc015569

Yackel, J. J., Barber, D. G., & Hanesiak, J. M. (2000). Melt ponds on sea ice in the Canadian Archipelago: 1. Variability in morphological and radiative properties. *Journal of Geophysical Research: Oceans*, *105*(C9), 22049–22060. https://doi.org/10.1029/2000jc900075

Zege, E., Malinka, A., Katsev, I., Prikhach, A., Heygster, G., Istomina, L., et al. (2015). Algorithm to retrieve the melt pond fraction and the spectral albedo of Arctic summer ice from satellite optical data. *Remote Sensing of Environment*, *163*, 153–164. https://doi.org/10.1016/j.rse.2015.03.012

Zhang, J., Schweiger, A., Webster, M., Light, B., Steele, M., Ashjian, C., et al. (2018). Melt pond conditions on declining Arctic sea ice over 1979–2016: Model development, validation, and results. *Journal of Geophysical Research: Oceans*, *123*(11), 7983–8003. https://doi.org/10.1029/2018jc014298

References From the Supporting Information

Fuchs, N. (2023). PASTA-ice. *Zenodo*. https://doi.org/10.5281/zenodo.7548469

Huang, W., Lu, P., Lei, R., Xie, H., & Li, Z. (2016). Melt pond distribution and geometry in high Arctic sea ice derived from aerial investigations. *Annals of Glaciology*, *57*(73), 105–118. https://doi.org/10.1017/aog.2016.30